A Square-Wave-Fed Bipolar Hybrid Cockcroft-Walton Voltage Multiplier for Aerospace Ionic Propulsion Power Supplies

SARA BALDISSERRI, Graduate Student Member, IEEE
RICCARDO MANDRIOLI, Senior Member, IEEE
GABRIELE NERETTI
MATTIA RICCO, Senior Member, IEEE
University of Bologna, Bologna, Italy

This article investigates a square-wave-fed bipolar hybrid Cockcroft–Walton voltage multiplier (BHY-VM) intended for high-voltage power supplies in ionic propulsion applications. The proposed topology combines the advantages of both bipolar and hybrid architectures. The electrical behavior of the BHY-VM is analytically characterized, including diode voltage drops, and compared with conventional VM configurations in terms of component count and ratings, Thévenin-equivalent parameters, and power losses. The square-wave excitation eliminates the need for a resonant magnetic interface while substantially modifying the charge-transfer mechanism. Experimental measurements validate the analytical model and confirm the predicted steady-state behavior of the proposed architecture over a wide operating range.Application-oriented considerations relevant to ionic propulsion power supplies are also discussed. In particular, the reduced output impedance and bipolar structure of the proposed BHY-VM support improved voltage regulation and reduced insulation requirements. Moreover, integration aspects, including gain distribution between transformer and VM stages, and high-voltage implementation constraints, are finally outlined for representative lightweight aerospace applications.

Received 2 March 2026; revised 3 June 2026; accepted 25 July 2026. Date of publication 29 July 2026; date of current version 19 August 2026.

DOI. No. 10.1109/TAES.2026.3718405

Refereeing of this contribution was handled by W. W. Weaver.

This work was supported by IPROP project that has received funding from the European Union's Horizon Europe Research and Innovation Programme under Grant 101098900.

Authors' addresses: Sara Baldisserri, Riccardo Mandrioli, Gabriele Neretti, and Mattia Ricco are with the Department of Electrical, Electronic and Information Engineering, University of Bologna, 40136 Bologna, Italy, E-mail: (sara.baldisserri2@unibo.it; r.mandrioli@unibo.it; gabriele.neretti@unibo.it; mattia.ricco@unibo.it). *(Corresponding author: Riccardo Mandrioli.)*

© 2026 The Authors. This work is licensed under a Creative Commons Attribution 4.0 License. For more information, see https://creativecommons.org/licenses/by/4.0/

I. INTRODUCTION

Advances in ionic propulsion technology are leading to developments in several fields, including aviation, climate monitoring, telecommunications, and other stratospheric missions [1], [2]. Preliminary sizing studies of air and space platforms employing ionic propulsion indicate operating voltages ranging from a few kilovolts for small-scale platforms to several tens of kilovolts for large demonstrators, with corresponding power levels from tens of watts up to kilowatts, while maintaining output currents in the microampere-to-milliampere range [3], [4], [5], [6]. Such scaling preserves the same underlying operating principles and electrical load characteristics.

The development of high-power-density high-voltage power electronic circuits plays a crucial role in the ionic thrusters' potential employment [7], [8]. There are two basic approaches generally used to generate DC high voltages. The first approach involves a high-turn-ratio transformer and high-breakdown-voltage diodes. However, the high-voltage transformer has several nonidealities that cause voltage and current spikes, leading to losses and noise. The second approach employs a high-frequency inverter, a transformer, and a Cockcroft–Walton voltage multiplier (VM) [9], [10], [11]. By using a VM, the turns ratio of the transformer, and thus the nonidealities mentioned above, can be significantly reduced. In addition, VM circuits are characterized by high voltage step-up ratio, low voltage stress on components, compactness, and easy implementation [12].

Among the various VM topologies, symmetrical configurations have been extensively investigated to mitigate the high output voltage ripple and drop that characterize conventional half-wave solutions [12]. The full-wave (FW) topology achieves this goal by adding an oscillating column of capacitors and a stack of diodes, but requires a center-tapped supply which increases the complexity of the system and could cause an asymmetry in the driving voltages, leading to harmonic generation in the DC output voltage [13], [14], [15]. To overcome this limitation, the hybrid (HY) VM gets rid of the center-tapped supply and the first oscillating capacitors [16], [17]. In addition, the bipolar approach was introduced to achieve a significant reduction in the high-voltage isolation requirements. The bipolar VMs consist in the connection of a positive and a negative bridge, improving the dynamic response and the voltage regulation of the system [18], [19] . The bipolar HY (BHY) VM, recently introduced by the authors in [20], represents the bipolar version of the HY-VM and combines the advantages of both bipolar and HY architectures. It fills the gap in the general framework of VMs and their respective bipolar topologies. Additional solutions for ionic propulsion applications have also been investigated by the authors, including architectures with multiple intermediate loads [21].

Until now, VMs have been analyzed by considering a sine wave input voltage [12]. This approach, however, introduces significant weight and complexity into the overall system due to the transformer and the resonant tank [7]. A different operating framework was recently proposed by the authors in [22] and [23], showing that the VM can be directly supplied by the inverter, thus eliminating the need for a resonant magnetic interface and substantially modifying the charge-transfer mechanism. Building upon this concept, this article investigates the application of square-wave operation to the BHY-VM, providing a more comprehensive analytical VM characterization considering diode voltage drops, analytical loss derivation, and a Thévenin-equivalent interpretation. Optional voltage step-up or galvanic isolation may still be introduced if required by the specific application. The proposed approach introduces an additional degree of freedom in the front-end design, enabling flexible frequency modulation and advanced control strategies.

When adopted as the high-voltage stage of a propulsion power processing unit (PPU), the VM is required to operate in a context where electrical behavior is dictated by the load rather than by the converter itself [24], [25]. Ionic thrusters behave as self-sustained nonlinear high-voltage loads whose operating point is defined by the intersection between the PPU and the thruster $I-V$ characteristics [26], [27]. The load can be interfaced either in single-ended or differential configuration and does not require actively driven high-voltage electrodes, thus eliminating the need for floating gate drivers at the output stage [5]. Although the actual ionic thruster follows a nonlinear law, its essential feature is to behave as a voltage-controlled load with limited current demand. In this perspective, both constant-current models and resistive loads are reasonable approximations of the thruster behavior, while enabling a straightforward and safe laboratory implementation.

Insulation coordination and electric-field distribution become primary design constraints [28]. In these systems the accelerating voltage determines thrust, making stable average output voltage and limited ripple critical constraints [3], [4], [5]. Consequently, converter output impedance, predictable transient behavior, and robustness to operating variations are key design parameters [29]. At the same time, air and space platforms impose severe constraints in terms of mass, volume, and insulation, favoring architectures capable of distributing the voltage stress and minimizing magnetic components [6], [7]. Within this framework, the BHY-VM is advantageous as it splits the total output voltage and improves regulation and ripple performance compared to conventional implementations [5], [18], [19]. However, square-wave operation introduces high current peaks in the VM stages, requiring appropriate component rating and careful tradeoffs between electrical performance, insulation, and weight. For this reason, the proposed topology is analyzed under application-relevant operating conditions [24], [25], [29].

From now on, the notation $|^{\mathrm{VM}}_{\mathrm{sin/sq}}$ will be used; the subscript refers to the input voltage waveform type (i.e., "sin" and "sq" in case of sine or square waves, respectively),

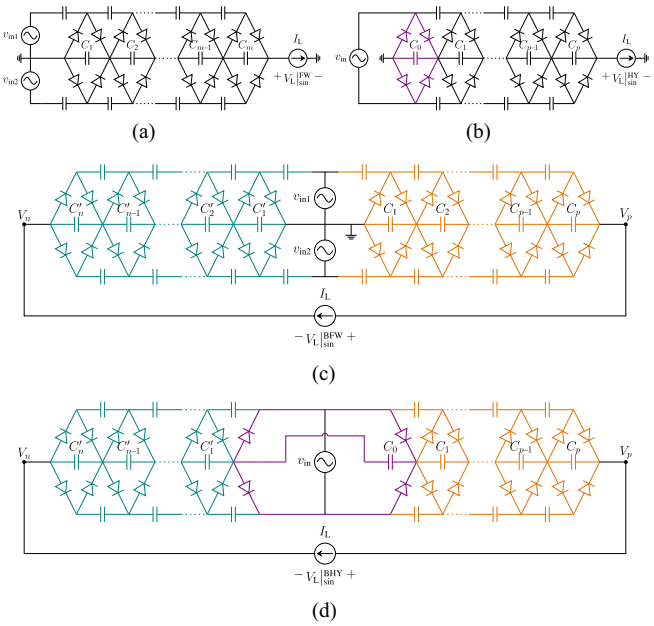

Fig. 1. (a) FW-VM. (b) HY-VM: diode bridge in violet and p-stage FW-VM; $p+1=m$. (c) BFW-VM: p-stage positive FW-VM in orange and n-stage negative FW-VM in teal; $p+n=m$. (d) m-stage BHY-VM: p-stage positive FW-VM in orange, n-stage negative FW-VM in teal, and shared diode bridge in violet; $p+n+1=m$.

while the superscript refers to the VM topology (i.e., "FW," "HY," "BFW," or "BHY" in case of FW-, HY-, BFW-, or BHY-VMs, respectively).

The rest of this article is organized as follows: Section II provides a background on symmetrical VMs, while Section III introduces the proposed square-wave-fed BHY-VM. Section IV derives the analytical power loss formulation and compares the proposed topology with conventional VM configurations. Section V provides the experimental validation. Section VI discusses application-oriented considerations. Finally, Section VII concludes this article.

II. BACKGROUND ON SINE-WAVE-FED SYMMETRICAL VMS

Fig. 1 summarizes the most common symmetrical VMs. The m-stage FW- and the BFW-VMs are driven by a pair of phase-shifted AC voltage sources $v_{\mathrm{in1}}=(V_{\mathrm{in}}/2)\sin(\omega t)$ and $v_{\mathrm{in2}}=(V_{\mathrm{in}}/2)\sin(\omega t-\pi)$, usually obtained by using a center-tapped supply, while the m-stage HY-VM is driven by an input AC voltage source $v_{\mathrm{in}}=V_{\mathrm{in}}\sin(\omega t)$. Their circuit topologies, steady-state operation, and analytical modeling under sine-wave excitation were comprehensively addressed by the authors in [20] and are therefore not repeated here. Differently from [20], the effect of the diode forward voltage drop V_{D} is here explicitly included. For analytical tractability, it is assumed that the load is a constant current I_{L}, and C is the capacitance of each capacitor.

The average output voltage of the uppermentioned sine-wave-fed VMs can be expressed as

$$\overline{V}_{\mathrm{L}}|^{\mathrm{FW}}_{\mathrm{sin}} = m(V_{\mathrm{in}}-2V_{\mathrm{D}})-\frac{1}{2fC}\left(\frac{m^3}{3}+\frac{m^2}{2}+\frac{2m}{3}\right)I_{\mathrm{L}} \quad (1)$$

$$\overline{V}_{\mathrm{L}}\big|_{\mathrm{sin}}^{\mathrm{HY}} = m(V_{\mathrm{in}} - 2V_{\mathrm{D}}) - \frac{1}{2fC}\left(\frac{m^3}{3} - \frac{m^2}{2} + \frac{2m}{3}\right) I_{\mathrm{L}} \quad (2)$$

$$\overline{V}_{\mathrm{L}}\big|_{\mathrm{sin}}^{\mathrm{BFW}} = \underbrace{m(V_{\mathrm{in}} - 2V_{\mathrm{D}})}_{V_{\mathrm{th}}} - \underbrace{\frac{1}{2fC}\left(\frac{m^3}{12} + \frac{m^2}{4} + \frac{2m}{3}\right)}_{R_{\mathrm{th}}} I_{\mathrm{L}} \quad (3)$$

where $f = 1/T$ is the AC voltage frequency. The obtained expression admits a Thévenin-equivalent interpretation. In this representation, the no-load output voltage corresponds to the Thévenin voltage source V_{th}, which explicitly incorporates V_{D}, whereas the coefficient multiplying I_{L} defines an equivalent lossless output resistance R_{th}, accounting for the voltage drop associated with capacitor charge redistribution during the charge-transfer process. This interpretation separates the static voltage drop due to diode nonidealities from the load-dependent regulation mechanism governed by R_{th}, providing a compact circuit-level insight into the steady-state behavior of the VMs.

A. Sine-Wave-Fed BHY-VM

The m-stage sine-wave-fed BHY-VM introduced by the authors in [20] is shown in Fig. 1(d); it consists of a p-stage positive FW-VM in orange, a n-stage negative FW-VM in teal, and a shared diode bridge in violet, where $p + n + 1 = m$. The formulation in [20] included two diode-bridge smoothing capacitors. This arrangement increases ripple and the associated average voltage drop without contributing to the charge-redistribution mechanism underlying the voltage multiplication process; therefore, only one diode-bridge smoothing capacitor C_0 is retained here. The two bridges are connected to the AC voltage source $v_{\mathrm{in}} = V_{\mathrm{in}} \sin(\omega t)$, and the load is connected between the positive and negative output terminals.

In steady-state operation, the capacitors of the smoothing column are charged in parallel by the oscillating columns and discharged in series through the load, twice every input voltage cycle. At no load, each capacitor of the smoothing column will charge up to the maximum value of the input voltage V_{in}. Thus, the total output voltage of the BHY-VM at no load is

$$V_{\mathrm{L}}\big|_{\mathrm{sin}}^{\mathrm{BHY}} = mV_{\mathrm{in}} - 2mV_{\mathrm{D}}. \quad (4)$$

If load current $I_{\mathrm{L}} > 0$, four main time intervals within a period T can be distinguished. Due to the half-wave symmetry of the symmetrical VMs, the analysis can be limited to the half period $T/2$ including the time intervals:

1) t_1 – the smoothing column capacitors are charged by the upper oscillating column; and
2) t_2 – the smoothing column capacitors are discharged through the load.

Fig. 2 represents the working principle of the sine-wave-fed BHY-VM during t_1 and t_2. As frequently done in literature, to analyze the VM circuits it can be assumed that the time interval $t_1 \ll T$. Therefore, the charging process t_1 is considered instantaneous and the discharging process lasts $t_2 = T/2$. This allows the portion of charge supplied

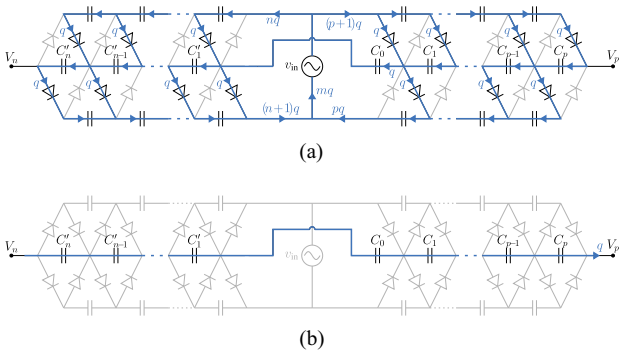

Fig. 2. Operating principle of the sine-wave-fed BHY-VM during (a) charging interval t_1 and (b) discharging interval t_2.

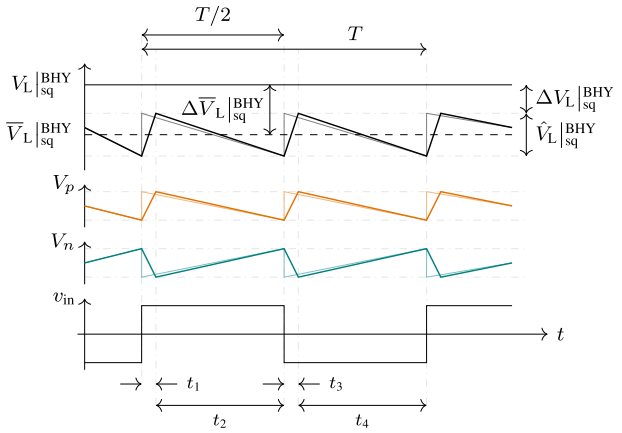

Fig. 3. Key steady-state waveforms of the square-wave-fed BHY-VM.

to the load during the charging interval t_1 to be neglected, and consider the load supplied only during interval t_2. Furthermore, this allows the obtaining of generic formulations that can give good approximation results regardless of the actual voltage waveform, capacitor size, and load value.

Considering that $q = I_{\mathrm{L}}/(2f)$ is the charge transferred to the load in $T/2$, with a simple power balance equation it can be obtained that the charge supplied by the source in time $T/2$ is $q_{\mathrm{in}} = mq$, as can also be deduced from Fig. 2.

As shown in [20] and adding the contribution of V_{D}, the average output voltage of the sine-wave-fed BHY-VM can be calculated as

$$\overline{V}_{\mathrm{L}}\big|_{\mathrm{sin}}^{\mathrm{BHY}} = \underbrace{m(V_{\mathrm{in}} - 2V_{\mathrm{D}})}_{V_{\mathrm{th}}} - \underbrace{\frac{1}{2fC}\left(\frac{m^3}{12} + \frac{5m}{12}\right)}_{R_{\mathrm{th}}} I_{\mathrm{L}}. \quad (5)$$

III. PROPOSED SQUARE-WAVE-FED BHY-VM

One of the main differences from the sinusoidal case is the topology of the VM. The diode bridge rectifies the input voltage v_{in}, while the smoothing capacitor C_0 is needed to hold the voltage at the value V_{in}. Since rectifying a square wave already yields a constant value, in this proposed approach, the diode-bridge smoothing capacitor C_0 can be removed.

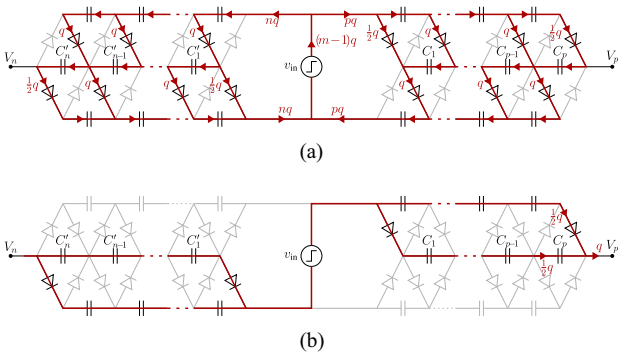

Fig. 4. Operating principle of the square-wave-fed BHY-VM during (a) charging interval t_1 and (b) discharging interval t_2.

Fig. 3 shows the key steady-state waveforms, while Fig. 4 represents the main operating principle of the square-wave-fed BHY-VM. As pointed out in Section II-A, the output voltage of the BHY-VM presents a half-wave symmetry; therefore, in the analysis, it can be considered only the smoothing column capacitors' charging interval t_1 and discharging interval t_2. At no load, with $I_L = 0$, the operating principle is the same as the sine case. Consequently, the total output voltage at no load is

$$V_L\Big|_{sq}^{BHY} = V_L\Big|_{sin}^{BHY} = mV_{in} - 2mV_D. \tag{6}$$

As shown in Fig. 4, $2p+1$ and $2n+1$ diodes conduct in the positive and negative bridges, respectively, during the analyzed half a period. Consequently, the voltage drop due to the diodes results to be $2mV_D$.

In presence of a load current $I_L > 0$, the square-wave-fed BHY-VM behaves differently from the sine case: during t_2 the input voltage is constant. This causes the conduction of the diode in the last stage of the multiplier chain, as shown in Fig. 4(b). It is easy to demonstrate that the charge supplied to the load during t_2 is equally shared between the smoothing and oscillating column capacitors. In fact, by looking at Fig. 4(b), it is clear that the circuit behaves like a capacitive current divider where the impedance of the two branches are equal.

The assumption $t_1 \ll T/2$ is particularly true in the square wave approach. The modified waveforms according to this approach are shown in mild colors in Fig. 3.

Similarly to the sinusoidal approach, it can be verified from Figs. 2 and 4 that the total charge supplied by the source in time $T/2$ is $q_{in} = mq$, where $q = I_L/(2f)$ is the charge transferred to the load in a period $T/2$.

A. Output Voltage Ripple

A charge variation equal to $q/2$ occurs on each smoothing column capacitor during t_2, as shown in Fig. 4(b). During t_1, they are charged back with the same amount of charge $q/2$ that they lost during the previous interval, as shown in Fig. 4(a). Therefore, the peak-to-peak ripple produced across each smoothing column capacitor is $q/(2C)$. The output voltage ripple of the positive bridge can be obtained by summing the individual voltage ripples of each smoothing column capacitor as

$$\hat{V}_p\Big|_{sq}^{BHY} = q\sum_{i=1}^{p}\frac{1}{2C_i} = \frac{q}{2C}p. \tag{7}$$

Owing to the symmetry of the topology, the same expression holds for the negative bridge by replacing p with n. Therefore, the total output voltage ripple is

$$\hat{V}_L\Big|_{sq}^{BHY} = \frac{q}{2C}(p+n) = \frac{q}{2C}(m-1). \tag{8}$$

B. Output Voltage Drop

The total output voltage drop of the square-wave-fed BHY-VM is the sum of the output voltage drops of the positive and negative bridges. These drops can be determined by finding the sum of the individual voltage drops of each smoothing column capacitor. Considering the positive bridge, during t_1 the first upper oscillating capacitor charges the smoothing capacitor C_1, which consequently can not have a voltage greater than

$$V_{C_1}\Big|_{sq}^{BHY} = V_{in} - \frac{q}{C}\left(p - \frac{1}{2}\right) \tag{9}$$

this applies to all the capacitors in the positive smoothing column. Given that capacitor C_p is charged by the whole upper oscillating column, its maximum voltage results to be

$$V_{C_p}\Big|_{sq}^{BHY} = V_{in} - \frac{q}{C}\left[\left(p-\frac{1}{2}\right)+\left(p-\frac{3}{2}\right)+\cdots+\frac{1}{2}\right]. \tag{10}$$

By summing all the obtained contributions, it is possible to compute the general formula for the output voltage drops of the positive bridge

$$\Delta V_p\Big|_{sq}^{BHY} = \frac{q}{C}\left[-\frac{1}{2}\sum_{i=1}^{p} i + \sum_{i=1}^{p} i^2\right] = \frac{q}{C}\left(\frac{p^3}{3}+\frac{p^2}{4}-\frac{p}{12}\right). \tag{11}$$

The same expression holds for the negative bridge by replacing p with n. The total output voltage drop is

$$\Delta V_L\Big|_{sq}^{BHY} = \frac{q}{C}\left(\frac{p^3+n^3}{3}+\frac{p^2+n^2}{4}-\frac{p+n}{12}\right) \tag{12}$$

C. Average Output Voltage

The average output voltage of the square-wave-fed BHY-VM can be calculated from (6), (8), and (12), as $\overline{V}_L = V_L - \Delta\overline{V}_L = V_L - (\Delta V_L + \hat{V}_L/2)$, where $\Delta\overline{V}_L = R_{th}I_L$ indicates the average output voltage drop

$$\overline{V}_L\Big|_{sq}^{BHY} = m(V_{in}-2V_D) - \frac{q}{C}\left[\frac{p^3+n^3}{3}+\frac{p^2+n^2}{4}+\frac{p+n}{6}\right] \tag{13}$$

and if $p = n = (m-1)/2$, (13) simplifies in

$$\overline{V}_L\Big|_{sq}^{BHY} = \underbrace{m(V_{in}-2V_D)}_{V_{th}} - \underbrace{\frac{1}{2fC}\left(\frac{m^3}{12}-\frac{m^2}{8}+\frac{m}{6}-\frac{1}{8}\right)}_{R_{th}}I_L. \tag{14}$$

IV. DISCUSSION AND COMPARISON

A. Considerations on Power Losses

Power losses generation mechanism in VMs is mainly driven by diode forward voltage drop V_D, diode equivalent resistance R_D, diode reverse recovery (RR) charge Q_{rr}, and capacitor equivalent series resistance (ESR) R_C . To simplify the derivation, assumptions $t_1 = t_3$ and $t_2 = t_4 \approx T/2$ are applied. In addition, given the impulsive nature of charging events during t_1 and t_3, the current shape is assumed to be triangular-like. Therefore, for an event of charge q, the average current is $\bar{I}_1 = q/t_1$ while its rms value is $\tilde{I}_1 = 2\bar{I}_1/\sqrt{3}$. On the other hand, slow discharging events during t_2 and t_4 are modeled as a constant current of value $\bar{I}_2 = q/t_2$. Weighting each contribution according to the charge amount displayed in Figs. 2 and 4, average losses P_{VM} within one period T are according to (15) shown at the bottom of this page. For the sake of completeness, one should add to (15) the contribution due to RR losses which is particularly relevant in non-Schottky diodes when high values of f and V_{in} are employed. Specifically, RR losses can be approximated as

$$P_{rr}\Big|_{\text{sin/sq}}^{\text{BHY}} \approx 4mQ_{rr}V_{in}f. \tag{16}$$

Neglecting low-order terms, considering that at high current $R_D \to 0$, replacing $I_L = P_L/V_L$, assuming $V_D \ll V_{in}$, and including (16), leads to the simplified formulation

$$P_{VM}\Big|_{\text{sin/sq}}^{\text{BHY}} \approx \underbrace{4mQ_{rr}V_{in}f}_{k_0} + \underbrace{2\frac{V_D P_L}{V_{in}}}_{k_1 P_L} + \underbrace{\frac{1}{9}\frac{P_L^2}{t_1 f}\frac{R_C}{V_{in}^2}m}_{k_2 P_L^2} \tag{17}$$

introduced to provide a practical approximation of the dominant power losses (i.e., diode forward voltage drop V_D, and capacitor ESR R_C) as a function of the output power P_L, while neglecting low-order terms that have a marginal impact under typical conditions. High-frequency solutions present a lower amount of charge q to be restored and therefore smaller current spikes. Systems whose parasitics or operating principle (e.g., sine-wave-based VMs) lead to a larger interval t_1 exhibit inherently smaller capacitive losses. Systems based on Schottky diodes (e.g., SiC diodes) generally present a negligible RR charge Q_{rr}, and therefore the term k_0 is often inconsequential. Increasing the number of stages m leads to a linear increment of capacitive (term $k_2 P_L^2$) and RR losses (term k_0) while diode forward voltage losses (term $k_1 P_L$) can be considered m-invariant.

Clearly, the closed-form solutions provide useful insights on losses but cannot represent in a perfect way the diode nonlinearity, parasitic effects, and temperature changes. To enlarge validity bracket, one could explore the probabilistic space of solutions employing a Monte Carlo approach varying all the above parameters across their tolerance diapason. Moreover, losses estimation should be assisted by measurement campaigns or at least SPICE simulations tailored for the specific application and design under consideration.

B. Comparison With Conventional VM Topologies

The analytical developments presented in Sections II and III, and Section IV-A, enable a direct comparison between the considered VM topologies. Table I summarizes the main characteristics of the state-of-the-art and proposed VM solutions in terms of component count and ratings, Thévenin-equivalent parameters, and power losses.

As shown, all the considered VMs exhibit a comparable number of diodes n_D and capacitors n_C, and identical component voltage-rating requirements, namely V_{in}. Current stress in the VMs is associated with the charge-transfer events occurring during the charging intervals $t_1 = t_3$. The actual peak current I_{pk} associated with an event of charge q depends on circuit parasitics and switching dynamics and is therefore not directly predicted by the analytical model. Considering the assumption introduced in Section IV-A, i.e., approximating the charging current as a triangular waveform with a crest factor of $\sqrt{3}$, it follows $I_{pk} \approx I_L/(ft_1)$. High-frequency operation and longer t_1 values lead to reduced current spikes. Bipolar topologies preserve the same diode current stress of conventional topologies, while approximately halving the capacitor current stress.

In practical implementations, current stress can be mitigated through device paralleling, commonly adopted to increase current capability while improving reliability and fault tolerance. Nevertheless, appropriate design considerations are required to ensure proper current sharing among parallel devices.

For what concerns the Thévenin-equivalent parameters, the considered VMs exhibit the same equivalent output voltage V_{th}, while significantly different equivalent output resistance R_{th} [see (1)–(3), (5), and (14)]. For the sake of brevity, Table I shows the normalized equivalent output resistance N_{th} (corresponding to the normalized average output voltage drop), according to $N_{th} = 2fCR_{th} = 2fC\Delta\bar{V}_L/I_L$. Such normalization provides a compact and technology-independent comparison of the

$$\begin{aligned} P_{VM}\Big|_{\text{sin}}^{\text{BHY}} &= 2mV_D I_L + \frac{4}{3}\frac{I_L^2}{t_1 f}\left[R_D m + R_C\left(\frac{m^3}{12} + \frac{5m}{12}\right)\right] + I_L^2 R_C m \approx 2mV_D I_L + \frac{1}{9}\frac{I_L^2}{t_1 f}R_C m^3 \\ [4pt] P_{VM}\Big|_{\text{sq}}^{\text{BHY}} &= 2mV_D I_L + \frac{4}{3}\frac{I_L^2}{t_1 f}\left[R_D\left(m - \frac{3}{2}\right) + R_C\left(\frac{m^3}{12} - \frac{m^2}{8} + \frac{m}{6} - \frac{1}{8}\right)\right] + I_L^2 R_C\frac{m-1}{2} + R_D I_L^2 \approx 2mV_D I_L + \frac{1}{9}\frac{I_L^2}{t_1 f}R_C m^3 \end{aligned} \tag{15}$$

TABLE I
Performance Comparison of the State-of-the-Art and Proposed VM Topologies

Topology	Wave	n_D	Diode rating	n_C	Cap. rating	V_{th}	N_{th}	P_{VM}
FW	Sine[§]	$4m$	V_{in}, I_{pk}	$3m$	V_{in}, mI_{pk}	$m(V_{in}-2V_D)$	$\frac{m^3}{3}+\frac{m^2}{2}+\frac{2m}{3}$	(17) with $4\times k_2P_L^2$
HY	Sine	$4m$	V_{in}, I_{pk}	$3m-2$	V_{in}, mI_{pk}	$m(V_{in}-2V_D)$	$\frac{m^3}{3}-\frac{m^2}{2}+\frac{2m}{3}$	(17) with $4\times k_2P_L^2$
BFW	Sine[§]	$4m$	V_{in}, I_{pk}	$3m$	V_{in}, $\frac{m}{2}I_{pk}$[†]	$m(V_{in}-2V_D)$	$\frac{m^3}{12}+\frac{m^2}{4}+\frac{2m}{3}$	(17)
BHY	Sine	$4m$	V_{in}, I_{pk}	$3m-2$	V_{in}, $\frac{m+1}{2}I_{pk}$[†]	$m(V_{in}-2V_D)$	$\frac{m^3}{12}+\frac{5m}{12}$	(15)-(17)
	Square	$4m$	V_{in}, I_{pk}	$3m-3$	V_{in}, $\frac{m-1}{2}I_{pk}$[†]	$m(V_{in}-2V_D)$	$\frac{m^3}{12}-\frac{m^2}{8}+\frac{m}{6}-\frac{1}{8}$	(15)-(17)

[§] Require center-tapped supply; [†] Considering $p=n$.

TABLE II
Numerical and Experimental Plant Parameter Values

Parameter	Symbol	Sim.	Exp.	
			Square	Sine
Input voltage	V_{in}	50 V	25-50 V	10-70 V
Frequency	f	10 kHz	0.1-10 kHz	40-60 kHz
Load current	I_L	0.01 A	-	
Load resistance	R_L	-	250, 500 kΩ	
Stages	m	1-10	1-10	
Capacitance	C	1 μF	1 μF	
CRV	V_R	-	1.1 kV	
ESR	R_C	36.5 mΩ	36.5 mΩ	
DOR	R_D	10 mΩ	10 mΩ	
DFV	V_D	0.7 V	0.7 V	
DRV	V_{RRM}	-	2.2 kV	

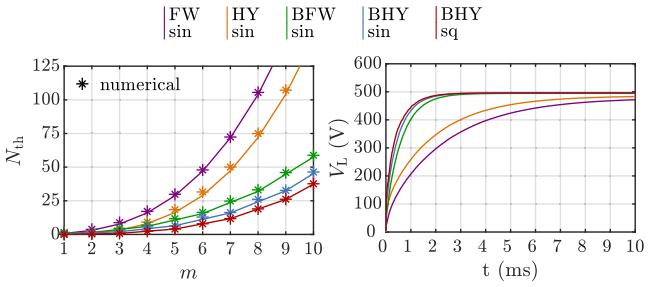

Fig. 5. Comparison of N_{th} (left) and numerical dynamic response for $m=10$ (right) of the analyzed VMs.

average output voltage drop, and consequently of the output voltage regulation capability. Bipolar VMs exhibit substantially reduced N_{th} values compared to conventional FW- and HY-VMs, and the proposed square-wave-fed BHY-VM achieves the lowest N_{th} among the considered solutions.

Section V-A will provide a numerical validation of N_{th} and of the related comparison, together with the dynamic response characteristics of the analyzed VMs.

Following the same approach adopted in Section IV-A for the proposed BHY-VM, analytical power-loss formulations can also be derived for the conventional VM topologies. In particular, the simplified loss expression of the BFW-VM coincides with that of the BHY-VM [see (17)], while the FW- and HY-VMs exhibit identical formulations characterized by a fourfold increase of the capacitive-loss contribution [i.e., (17) with $4\times k_2P_L^2$]. The same considerations regarding the influence of the main design parameters on VM losses also apply to the conventional VM configurations.

V. NUMERICAL AND EXPERIMENTAL VALIDATION

To highlight the different operating behavior of the considered VM topologies, a comparative numerical analysis is first presented. Moreover, the sine- and square-wave-fed BHY-VM have been tested experimentally. The employed parameters are summarized in Table II, where V_R is the capacitor rated voltage (CRV), R_D is the diode on-state resistance (DOR), and V_{RRM} is the diode peak repetitive reverse voltage (DRV). The simulation parameters are selected to keep the operating power level comparable to that of the experimental prototype. For simplicity, it is assumed that $p\geq n$, i.e., when m is even, the additional stage is placed in the positive bridge. Such an assumption does not limit result validity and proposal consistency.

A. Numerical Comparison

The sine-wave-fed FW-, HY-, BFW-, and BHY-VMs in Fig. 1, and the square-wave-fed BHY-VM are simulated in the PLECS (Plexim GmbH) environment. Fig. 5(left) shows N_{th} as a function of the total number of stages m. The square-wave-fed BHY-VM exhibits improved output voltage regulation, i.e., smaller load-dependent reduction of the average output voltage, resulting from reduced charge redistribution and consequently lower voltage drop and ripple. As shown, numerical results (asterisks) fairly match the analytical predictions (solid traces), with a mean relative error of 0.86% related to the proposed BHY topologies. Fig. 5(right) shows the numerical dynamic response in time of the analyzed VMs for $m=10$. It can be verified that bipolar topologies, and in particular the square-wave-fed BHY-VM, have a faster dynamic response.

B. Experimental Validation

The performance of the sine- and square-wave-fed BHY-VM are evaluated using the laboratory test branch

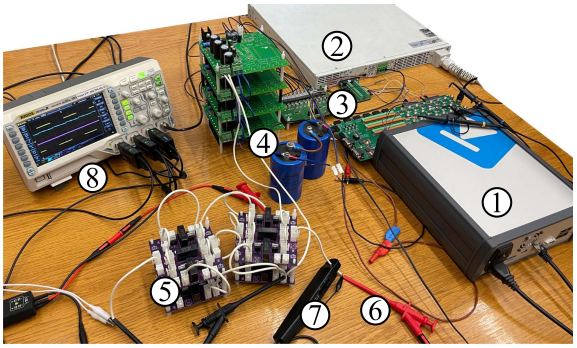

Fig. 6. Experimental test bench: (1) Plexim RT Box 1, (2) TDK-Lambda GEN1500 W adjustable power supply, (3) optical link, (4) split-capacitor inverter, (5) proposed BHY-VM, (6) Micsig DP series high-voltage differential probe, (7) Micsig MCP/CP series high-frequency AC/DC current probe, and (8) Rigol DS1054Z oscilloscope.

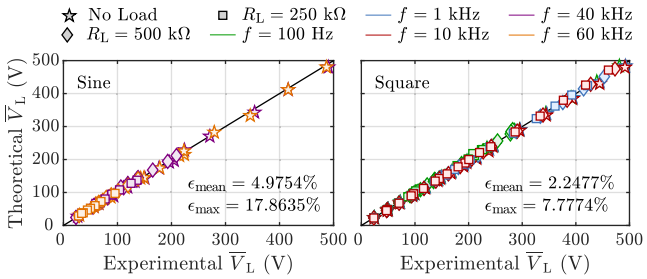

Fig. 7. Experimental validation of the average output voltage $\overline{V}_L$ of the sine- and square-wave-fed BHY-VM: theoretical versus measured values.

depicted in Fig. 6 and considering the parameters listed in Table II. A resistive load $R_L = \overline{V}_L/I_L$ is employed for simplicity and safety reasons. Resistive loads are reasonable approximations of the thruster behavior, while enabling a straightforward and safe laboratory implementation. The split-capacitor inverter is made from the insulated gate bipolar transistor (IGBT) power module PS22A76 (Mitsubishi Electric), and it is fed by a GEN1500 W (TDK Lambda) adjustable power supply. An RT Box 1 (Plexim), operated via PLECS External Mode, is used to drive the inverter, which feeds the square-wave-fed BHY-VM composed of DNA30E2200PA (Littelfuse) diodes and ECWFG1B105 J (Panasonic) capacitors. Voltages and currents are sensed using DP series high-voltage differential probes and MCP/CP series high-frequency AC/DC current probes (Micsig), respectively. Moreover, a high-voltage high-frequency sinusoidal power supply is used to generate the sinusoidal input voltage [30]. The generator architecture is based on a commercial low-voltage AC/DC converter feeding a push–pull high-voltage transformer. A TL494 (ON Semiconductor) integrated circuit generates the pulse width modulation (PWM) control signal to drive IRF3415 (International Rectifier) MOSFETs.

240 steady-state measurements of the sine- and square-wave-fed BHY-VM have been acquired for different experimental parameter conditions, and the theoretical versus experimental average output voltage

TABLE III
Experimental Efficiency of the Proposed Square-Wave-Fed BHY-VM

m	V_{in} (V)	f (kHz)	R_L (kΩ)	P_L (mW)	η (%)	
					Exp.	(17)±σ
10	25	0.1	500	38.2	77.1	74.5±1.5
10	25	10	500	103.7	43.4	39.9±2.2
10	50	0.1	500	157.4	76.2	76.5±1.5
10	50	10	500	444.8	40.7	39.6±2.3
10	50	0.1	250	179.5	62.5	62.0±2.2
10	50	1	250	709.2	84.3	83.6±1.2
10	50	10	250	837.3	42.7	41.4±2.4
7	25	1	500	52.2	82.8	81.4±1.1
7	25	10	500	51.6	35.8	36.3±2.1
7	50	1	500	225.0	80.6	78.8±1.5
7	50	10	500	227.7	35.7	35.5±2.2
5	25	10	500	27.8	32.9	32.8±2.0
5	50	10	500	123.0	35.5	32.1±2.1

$\overline{V}_L$ values are shown in Fig. 7. As shown, experimental results fairly match the analytical predictions for each load condition. The analytical model accurately predicts the measured behavior over the whole operating range. The square-wave operation exhibits improved predictability, with a mean relative error of 2.25% compared to 4.98% in sine-wave operation. This confirms the capability of the proposed analytical approach and highlights the more deterministic behavior of the square-wave-fed topology.

Fig. 8 shows the experimental steady-state input currents and output voltages of the square-wave-fed BHY-VM in some representative experimental parameter conditions. The current exhibits a pulsed waveform, with the pulses lasting t_1 and t_3. This confirms that the assumption $t_1 \ll T/2$ is valid, particularly in the square wave approach. The use of a square wave input voltage introduces high (order of A) current spikes due to fast capacitive transients. The theoretical voltage waveforms shown in Fig. 3 are validated. At no load, the output voltage ripple is zero, and the input currents are very low. By connecting the load, the output voltage ripple and drop increase as the input voltage and the number of stages increase. As the switching frequency increases, the output voltage ripple and the input current decrease, as predicted by the analysis.

C. Experimental Efficiency Discussion

VMs are generally characterized by moderate conversion efficiency due to repetitive charge redistribution mechanisms. However, in the considered aerospace ionic propulsion applications, efficiency is often not the primary design driver. As will be further discussed in Section VI, compactness, reduced insulation requirements, low weight, and system reliability are typically prioritized.

Table III reports the experimental efficiency η of the proposed square-wave-fed BHY-VM in some representative operating conditions, spanning from 33% to 84%. Such measurements are compared with the closed-form prediction reported in (17). RR charge Q_{rr} and charge interval t_1 are estimated from the experimental waveforms. To extend the validity bracket to include nonidealities and temperature-dependent effects, the calculation of losses is iterated 10 000 times according to a Monte Carlo approach, where each parameter has been treated as a normally distributed random variable with a three-sigma tolerance of ±5%. The resulting

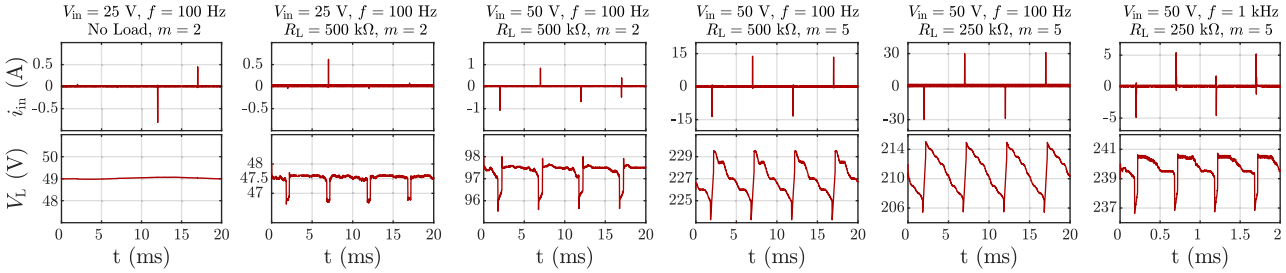

Fig. 8. Experimental steady-state input current and output voltage of the square-wave-fed BHY-VM for different experimental parameter values.

values reported in Table III represent the range within one standard deviation from the mean value, showing good agreement with the experimental measurements over the considered operating range.

At low frequencies (100 Hz) the low P_L results in an unfavorable ratio between useful power and fixed losses, particularly the V_D-related contribution (term $k_1 P_L$), resulting in intermediate efficiency values. At intermediate frequencies (1 kHz), the efficiency reaches its peak, up to 84%. The increase in P_L improves the overall loss-to-power ratio, RR losses (term k_0) remain moderate, and capacitive losses (term $k_2 P_L^2$) are not yet dominant, representing the best tradeoff among all considered cases. At higher frequencies (10 kHz), a sharp efficiency drop is observed across all operating conditions due to the conventional rectifier diodes (not Schottky) employed, resulting in nonnegligible RR losses. Moreover, a slight efficiency improvement is observed with increasing m, with lower R_L, and with higher V_{in}.

D. Expected Deviations With Ionic Thruster

The experimental validation is carried out using a resistive load in order to verify the electrical behavior of the proposed VM under controlled and repeatable conditions. An ionic thruster, however, does not behave as a purely resistive element. The discharge is characterized by an ignition voltage threshold subject to variability and noise, possible hysteresis between ignition and extinction, and operating regions where the incremental impedance may become negative due to plasma formation and sheath dynamics [4].

These effects mainly influence the local electrical response of the load rather than the capability of the high-voltage stage to establish an operating point. The converter investigated in this work behaves as a finite-output-impedance voltage source; therefore, variations of ignition voltage, emission conditions, or plasma operating mode primarily shift the equilibrium voltage but do not suppress it as long as the converter output resistance remains sufficiently low [24], [25], [29].

Moreover, the plasma–sheath interface introduces an intrinsic capacitive behavior that attenuates fast voltage variations. As a result, a real propulsion load is generally less sensitive to high-frequency voltage components than a purely resistive load, while slow dynamics dominate the discharge evolution. The application-oriented considerations discussed in the following section provide a qualitative perspective on the interaction between the proposed VM and representative propulsion loads [27].

VI. APPLICATION-ORIENTED CONSIDERATIONS FOR IONIC PROPULSION POWER SUPPLIES

This section discusses application-oriented considerations relevant to ionic propulsion power supplies.

A. Representative Operating Conditions

The representative propulsion load is assumed to operate at an output voltage $V_L = 2$ kV and power $P_L = 10$ W, corresponding to a nominal current $I_L = 5$ mA. Such conditions are consistent with low-power ionic propulsion implementations and represent an intermediate scale between laboratory demonstrators and high-altitude platforms.

A reference PPU architecture composed of a full-bridge inverter, a step-up transformer, and a BHY-VM is considered. A switching frequency $f = 50$ kHz is adopted as a compromise enabling compact passive components and limited output voltage ripple. The DC bus voltage $V_{DC} = 28$ V corresponds to a commonly adopted nominal low-voltage DC bus in embedded power systems. A transformer turns ratio of 1:15 is assumed, providing an intermediate voltage level at the VM input. The resulting peak voltage at the transformer secondary is $V_{in} = 420$ V. The number of VM stages is consequently set to $m = 5$, achieving the required output voltage under nominal conditions.

The representative PPU is simulated in the PLECS (Plexim GmbH) environment. Unless otherwise specified, the employed VM parameters correspond to those reported in Table II. A transformer including a series leakage inductance of 1.5 μ H and winding resistance of 200 mΩ is considered. The inverter switches are modeled as MOSFETs with integrated antiparallel diodes and ON-state resistance of 10 mΩ. The adopted models are intended to capture the dominant circuit-level nonidealities relevant to the considered operating conditions.

B. Thruster Model and Operating Point Stability

The ionic thrusters behave as voltage-controlled loads and can be modeled by a nonlinear voltage-controlled law, with a quadratic current–voltage relation above the emission threshold voltage V_0 and a nearly-cubic dependence of the absorbed power on the applied voltage

$$P(V) = KV^2(V - V_0) \tag{18}$$

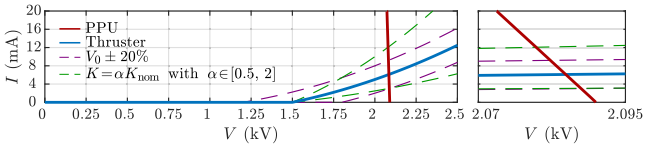

Fig. 9. $I-V$ characteristics of the PPU and thruster model.

where $V_0 = 1.5$ kV, and $K = 5 \times 10^{-9}$ A/V^2 is a constant coefficient identified from the nominal operating point.

Since the thruster behaves as a voltage-controlled nonlinear load, the operating point emerges from the interaction between the converter characteristic and the plasma $I-V$ curve, as shown in Fig. 9. The thruster model exhibits a well-defined emission threshold at V_0, below which the extracted current is negligible. Above V_0, the current increases rapidly with voltage, intersecting the PPU characteristic in the proximity of the nominal operating point. The intersection, therefore, represents a self-consistent accelerating voltage rather than a regulated setpoint [4], [26], [27].

Local stability of the operating point can be assessed through incremental analysis. The high-voltage stage can be approximated by a Thevenin equivalent source $V = V_{\text{th}} - R_{\text{th}} I$, leading to an incremental slope

$$\frac{dI_{\text{PPU}}}{dV} = -\frac{1}{R_{\text{th}}} = -1.25 \times 10^{-2} \text{ A/V}. \tag{19}$$

From (18), the thruster exhibits a voltage-dependent current, leading to the incremental slope

$$\frac{dI_{\text{thr}}}{dV} = K(2V - V_0) = 1.25 \times 10^{-5} \text{ A/V}. \tag{20}$$

The incremental stability condition can be written as

$$\frac{dI_{\text{PPU}}}{dV} + \frac{dI_{\text{thr}}}{dV} = -1.25 \times 10^{-2} + 1.25 \times 10^{-5} < 0 \tag{21}$$

indicating a stable operating point [24], [25], [29].

The robustness of the operating point with respect to propulsion parameter variations is further evaluated in Fig. 9, where the ignition voltage and emission coefficient are varied ($V_0 \pm 20\%$, $K = \alpha K_{\text{nom}}$ with $\alpha \in [0.5,\ 2]$). Parameter variations shift the operating point but do not alter its existence or stability.

C. On/Off PWM Control Strategy

The control strategy adopted for the proposed PPU is based on low-frequency ON/OFFmodulation of the inverter stage. Fast voltage regulation is avoided since it may interfere with plasma ignition and create oscillatory coupling with the discharge. In ionic propulsion, the dominant dynamics are governed by the vehicle mechanical response, whose time constants are much slower than the electrical dynamics of the PPU, making tight closed-loop regulation unnecessary for stable thrust generation. This approach simplifies implementation, avoids high-voltage sensing and fast feedback loops, and improves robustness against parameter variations.

Fig. 10(a) shows the simulated time-domain response of the PPU–thruster system under low-frequency ON/OFF

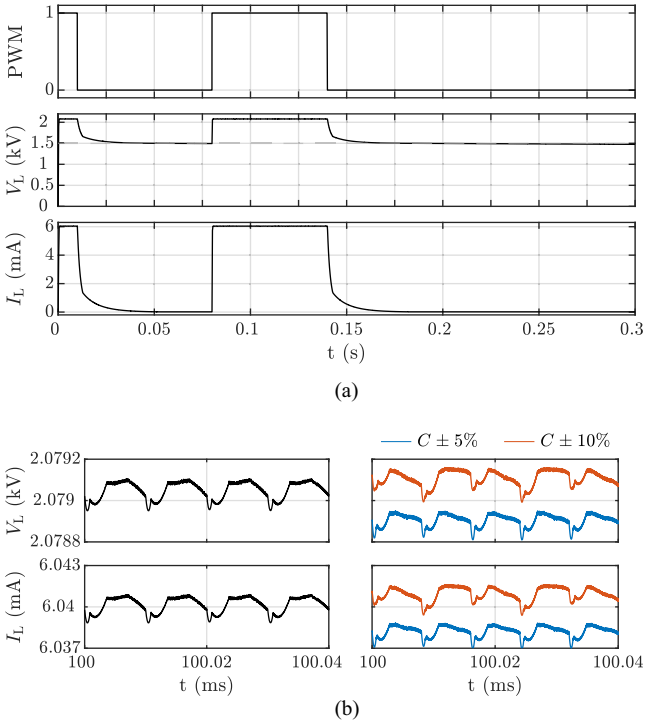

Fig. 10. (a) Simulated PWM signal, output voltage V_L, and thruster current I_L under ON/OFFoperation of the PPU. (b) Zoomed view of steady-state V_L and I_L under nominal conditions and with independent capacitance mismatches of $\pm 5\%$ and $\pm 10\%$.

PWM control. When the inverter is switched OFF, V_L decreases monotonically and the thruster current rapidly collapses, confirming the absence of oscillations or unstable behavior during turn-OFF. A subsequent re-energization event shows a smooth recovery of both voltage and current, with the system returning to the same operating point without overshoot or undesired reignition. The repeated ignition and extinction events can be interpreted as a large-signal perturbation of the propulsion load characteristic. During extinction, the load current collapses and the operating point temporarily disappears, while during reignition the nonlinear $I-V$ curve is abruptly reintroduced. The response shows convergence toward the same steady operating point without bistable or runaway regimes, indicating robustness against moderate variations of discharge conditions, such as pressure or emission fluctuations [4], [27].

As shown in Fig. 10(b), at steady state, the peak-to-peak voltage ripple is approximately 0.2 V over a nominal voltage of 2 kV, corresponding to about 0.01%. Additional simulations are performed considering independent capacitor tolerances of $\pm 5\%$. The mismatch slightly perturbs the local charge-redistribution dynamics, introducing a mild cycle-to-cycle waveform asymmetry, while the peak-to-peak accelerating-voltage ripple remains practically unchanged. Even when extending the tolerance range to $\pm 10\%$, no significant degradation of the operating behavior is observed. This confirms that the proposed converter operates well within the stringent ripple constraints typically associated with ionic propulsion.

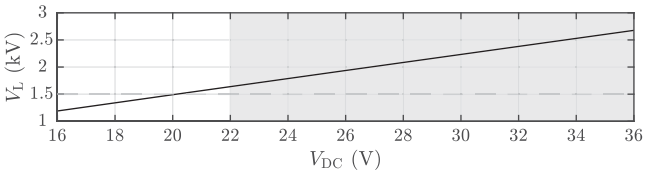

Fig. 11. Steady-state accelerating voltage versus input DC bus voltage.

A detailed inspection of the turn-OFFtransient reveals the presence of two distinct discharge regimes. Immediately after inverter shutdown, a first transient dominates the dynamics. In this phase, the voltage decay is governed by the equivalent capacitance of the VM $C_{eq} = C/m = 20$ nF and by the electrical behavior of the active thruster. In the operating region above the ignition threshold, the thruster exhibits an approximately linear $I-V$ characteristic, corresponding to an incremental resistance of about 100 kΩ. A local characteristic time constant $\tau \approx 2$ ms can be identified immediately after inverter shutdown. However, due to the strongly nonlinear nature of the thruster $I-V$ characteristic, the incremental resistance increases rapidly as the voltage decreases, the discharge progressively slows down and the overall duration of the first transient extends over about 40 ms. As the voltage decreases, the thruster current diminishes continuously and the incremental resistance increases sharply. Once the thruster resistance becomes comparable to or larger than the bleed resistance, the dominant discharge path shifts accordingly and a second, significantly slower discharge regime becomes apparent.

D. Aerospace Applicability and Design Constraints

The interaction between the propulsion load and the high-voltage stage must remain stable not only with respect to load variations but also with respect to variations of the DC bus [6]. In practical platforms the low-voltage bus is not tightly regulated and may deviate from its nominal value due to battery state-of-charge, solar array operating conditions, and distribution losses. To evaluate this aspect, the steady-state operating point is computed while sweeping the DC bus voltage in the range $V_{DC} = 16$–36 V, encompassing both degraded and overvoltage conditions. The resulting accelerating voltage V_L is reported in Fig. 11. The operating point varies approximately linearly with V_{DC}, as expected from the finite output resistance of the VM. However, V_L remains above V_0 for the entire nominal operating range around 28 V. Only for strongly reduced bus voltages approaching 20 V the operating point approaches the extinction condition. These results indicate that bus disturbances produce smooth and predictable shifts of the equilibrium voltage, without runaway or bistable regimes. As a consequence, variations of V_{DC} primarily translate into corresponding changes in delivered power and thrust level, while preserving the existence and local stability of the operating point. This behavior enables direct interfacing with typical onboard power buses without requiring tight preregulation.

Beyond electrical behavior, high-voltage implementation constraints become a primary design driver. The bipolar topology reduces the maximum potential difference with respect to ground, relaxing insulation requirements and facilitating integration in compact platforms [24], [29]. The required voltage gain can be distributed between the transformer and the VM stages, shifting part of the step-up from the magnetic interface to the electrostatic structure. This avoids excessive transformer turns ratios, reduces parasitics and mass, and distributes the electric field across multiple low-voltage elements. However, square-wave excitation introduces higher current peaks in the multiplier stages, requiring appropriate component rating and field management. The resulting design therefore consists of a tradeoff between transformer size, number of stages, and electrical stress, enabling scalable voltage adaptation while meeting insulation and integration constraints.

The following considerations refer only to the high-voltage generation stage; losses in the inverter and transformer depend on the specific implementation and are not included. According to (17), for the considered operating point, total VM losses remain well below a few watts and are distributed among the $m = 5$ stages. Assuming junction-to-ambient thermal resistances of 60–120 °C/W, the corresponding temperature rise is expected to remain within a few tens of degrees Celsius. Therefore significant localized hot spots are not expected and the topology is compatible with low-convection environments [7].

Environmental constraints typical of aerospace platforms must also be considered. In reduced-pressure environments, high-voltage operation is mainly limited by partial discharge inception. In the proposed BHY-VM, each stage is subjected approximately to the input peak voltage V_{in}. Assuming compact layouts with millimetric insulation spacing ($d \approx 3$ mm), the electric field is $E \approx V_{in}/d \approx 140$ V/mm, which remains well below breakdown levels predicted by Paschen's law in the pressure range relevant to aerial and near-space operation. The bipolar structure therefore relaxes insulation requirements and enables compact integration [28].

Square-wave excitation produces fast voltage transitions and impulsive charging currents. For a transition of amplitude V_{in} and rise time ≈ 100 ns, the slew rate is $dV/dt \approx 4 \times 10^9$ V/s and the displacement current in each stage capacitor is $I_{pk} = C\,dV/dt \approx 4$ A. These currents circulate locally between adjacent stages and mainly constitute differential-mode components. Due to the floating and compact structure of the VM, the radiation loop area is limited and radiated emissions are expected to be dominated by the primary inverter rather than the high-voltage generator itself. Therefore, the topology does not introduce qualitatively different EMI mechanisms compared to conventional isolated converters, although standard filtering and layout practices remain required [27].

These evaluations provide order-of-magnitude design indications rather than compliance verification, and are intended to guide integration choices rather than replace dedicated EMC and high-voltage qualification testing.

From an application perspective, the proposed architecture is best suited to voltage-dominated loads operating

at kilovolt levels and milliampere currents. Conversely, systems requiring tightly regulated high-power plasma discharges or large average currents may favor architectures optimized for continuous conduction and efficiency. The presented solution should therefore be regarded as a targeted approach for lightweight high-voltage propulsion power supplies rather than a universal high-voltage generator.

VII. CONCLUSION

This article analyzes a square-wave-fed BHY Cockcroft–Walton VM intended for high-voltage power supplies in ionic propulsion applications. The electrical behavior of the proposed topology was analytically derived, including diode voltage drops, Thévenin-equivalent parameters, and dominant loss mechanisms, and experimentally validated over a wide operating range with a mean relative error of 2.25%. The square-wave excitation eliminates the need for a resonant magnetic interface while substantially modifying the charge-transfer mechanism. Compared with conventional VM configurations, the proposed architecture achieves improved voltage regulation and reduced output ripple while preserving comparable component count and voltage stress. The bipolar structure also reduces insulation requirements and distributes the electrical stress across multiple stages, supporting compact high-voltage implementations. On the other hand, square-wave operation introduces higher instantaneous charging currents, requiring appropriate component sizing and careful management of parasitic effects. Application-oriented considerations relevant to ionic propulsion power supplies are finally discussed under representative operating conditions. The obtained results support the applicability of the proposed architecture to lightweight aerospace high-voltage systems operating with voltage-dominated loads.

ACKNOWLEDGMENT

Views and opinions expressed are, however, those of the authors only and do not necessarily reflect those of the European Union or EISMEA. Neither the European Union nor the granting authority can be held responsible for them.

REFERENCES

[1] L. Zhang, W. Zhu, H. Du, and M. Lv, "Multidisciplinary design of high altitude airship based on solar energy optimization," *Aerosp. Sci. Technol.*, vol. 110, 2021, Art. no. 106440.

[2] D. M. Goebel, I. Katz, and I. G. Mikellides, *Fundamentals of Electric Propulsion*. Hoboken, NJ, USA: Wiley, 2023.

[3] F. J. Blázquez-Plaza, A. Barrado, and M. Wijnen, "High-performance, miniaturized and configurable power and control unit for electrospray thrusters," *CEAS Space J.*, vol. 17, no. 2, pp. 273–291, 2025.

[4] F. J. Blázquez-Plaza, A. Barrado, M. Wijnen, and D. Villegas-Prados, "Electrical model and electrical temperature-dependent model for electrospray thrusters," *IEEE Trans. Power Electron.*, vol. 38, no. 10, pp. 12988–12998, Oct. 2023.

[5] H. Xu et al., "Flight of an aeroplane with solid-state propulsion," *Nature*, vol. 563, no. 7732, pp. 532–535, 2018.

[6] C. E. D. Riboldi et al., "Preliminary sizing of high-altitude airships featuring atmospheric ionic thrusters: An initial feasibility assessment," *Aerospace*, vol. 11, no. 7, pp. 590, 2024.

[7] Y. He and D. J. Perreault, "Lightweight high-voltage power converters for electroaerodynamic propulsion," *IEEE J. Emerg. Sel. Topics Ind. Electron.*, vol. 2, no. 4, pp. 453–463, Oct. 2021.

[8] N. Barsoum and G. I. Stanley, "Design of high voltage low power supply device," *Univ. J. Elect. Electron. Eng.*, vol. 3, no. 1, pp. 6–12, 2015.

[9] N. M. Waghamare and R. P. Argelwar, "High voltage generation by using Cockcroft–Walton multiplier," *Int. J. Sci. Eng. Technol. Res.*, vol. 4, no. 2, pp. 256–259, 2015.

[10] L. Müller and J. W. Kimball, "High gain DC–DC converter based on the Cockcroft–Walton multiplier," *IEEE Trans. Power Electron.*, vol. 31, no. 9, pp. 6405–6415, Sep. 2016.

[11] A. K. Sinha and R. Kumar, "Generation of high voltage using Cockcroft–Walton voltage multiplier circuit," *Int. Res. J. Eng. Technol.*, vol. 5, no. 1, pp. 510–513, 2018.

[12] M. Ruzbehani, "A comparative study of symmetrical Cockcroft–Walton voltage multipliers," *J. Elect. Comput. Eng.*, vol. 2017, no. 1, 2017, Art. no. 4805268.

[13] W. Heilpern, "Kaskadengeneratoren zur Partikelbeschleunigung auf 4 MeV," *Helvetica Physica Acta*, vol. 28, no. 5, pp. 485–491, 1955.

[14] G. Reinhold, K. Truempy, and J. Bill, "The symmetrical cascade rectifier an accelerator power supply in the megavolt and milliampere range," *IEEE Trans. Nucl. Sci.*, vol. 12, no. 3, pp. 288–292, Jun. 1965.

[15] H. Zhang and A. Takaoka, "Fundamental harmonic of ripples in symmetrical Cockcroft–Walton cascade rectifying circuit," *Rev. Sci. Instrum.*, vol. 67, no. 9, pp. 3336–3337, 1996.

[16] S. Iqbal, "A hybrid symmetrical voltage multiplier," *IEEE Trans. Power Electron.*, vol. 29, no. 1, pp. 6–12, Jan. 2014.

[17] V. Mudeng, H. S. Natiand, M. N. Farid, B. Hasanah, and V. A. Kusuma, "Performance analysis of hybrid symmetrical voltage multiplier using low pass filter," in *Proc. 10th Elect. Power, Electron., Commun., Controls Inform. Seminar*, 2020, pp. 193–197.

[18] S. Iqbal and R. Besar, "A bipolar Cockcroft–Walton voltage multiplier for gas lasers," *Amer. J. Appl. Sci.*, vol. 4, no. 10, pp. 795–801, 2007.

[19] S. Iqbal, R. Besar, and C. Venkataseshaiah, "Single/three-phase symmetrical bipolar voltage multipliers for X-ray power supply," in *Proc. Int. Conf. Elect. Eng*., 2008, pp. 1–6.

[20] S. Baldisserri, R. Mandrioli, G. Neretti, M. Ricco, and A. Cristofolini, "A bipolar hybrid symmetrical Cockcroft–Walton voltage multiplier for high-voltage DC power supplies," in *Proc. 51st Annu. Conf. IEEE Ind. Electron. Soc.*, 2025, pp. 1–6.

[21] S. Baldisserri, R. Mandrioli, G. Neretti, M. Ricco, and A. Cristofolini, "Symmetrical Cockcroft–Walton voltage multipliers with multiple intermediate loads for ionic propulsion in atmosphere," in *Proc. IEEE/AIAA Transp. Electrific. Conf. Electric Aircr. Technol. Symp.*, 2025, pp. 1–6.

[22] S. Baldisserri, R. Mandrioli, G. Neretti, M. Ricco, and A. Cristofolini, "Square-wave-fed Cockcroft–Walton voltage multipliers for ionic propulsion in atmosphere," in *Proc. IEEE/AIAA Transp. Electrific. Conf. Electric Aircr. Technol. Symp.*, 2025, pp. 1–6.

[23] S. Baldisserri et al., "Square-wave-fed hybrid symmetrical Cockcroft–Walton voltage multiplier for high-voltage DC power supplies," in *Proc. IEEE Int. Conf. Power Electron., Smart Grid, Renewable Energy*, 2025, pp. 1–5.

[24] R. D. Middlebrook and S. Cuk, "A general unified approach to modelling switching-converter power stages," in *Proc. IEEE Power Electron. Specialists Conf.*, 1976, pp. 18–34.

[25] S. D. Sudhoff, S. F. Glover, P. T. Lamm, D. H. Schmucker, and D. Delisle, "Admittance space stability analysis of power electronic systems," *IEEE Trans. Aerosp. Electron. Syst.*, vol. 36, no. 3, pp. 965–973, 2000.

[26] A. Krishnan et al., "Impedance analysis of the hall thruster discharge circuit and plasma load to address harness facility effects," in *Proc. 38th Int. Electric Propulsion Conf.*, 2024, Art. no. IEPC-2024-619.

[27] M. A. Lieberman and A. J. Lichtenberg, "Principles of plasma discharges and materials processing," *MRS Bull.*, vol. 30, no. 12, pp. 899–901, 1994.
[28] Y. Zhang, "A review of low-pressure and high-voltage insulation technology," in *Proc. 11th Frontier Academic Forum Elect. Eng.*, 2024, pp. 174–187.
[29] J. Sun, "Impedance-based stability criterion for grid-connected inverters," *IEEE Trans. Power Electron.*, vol. 26, no. 11, pp. 3075–3078, 2011.
[30] G. Neretti and M. Ricco, "Self-tuning high-voltage and high-frequency sinusoidal power supply for dielectric barrier discharge plasma generation," *Electronics*, vol. 8, no. 10, 2019, Art. no. 1137.

Sara Baldisserri (Graduate Student Member, IEEE) received the B.Sc. degree and the M.Sc. degree (cum laude) in electrical engineering from the Alma Mater Studiorum - University of Bologna, Bologna, Italy, in 2021 and 2023, respectively, where she is currently working toward the Ph.D. degree in biomedical, electrical, and system engineering, with the Power Electronic Circuits and Photovoltaics Group, Department of Electrical, Electronic, and Information Engineering.

Her research interests include high-power-density high-voltage DC/DC power electronic converters for ionic propulsion.

Riccardo Mandrioli (Senior Member, IEEE) received the Ph.D. degree (hons.) in biomedical, electrical, and system engineering from the University of Bologna, Bologna, Italy, in 2023.

He is currently a Tenure Track Assistant Professor of Electrical Engineering with the Department of Electrical, Electronic, and Information Engineering, University of Bologna. From 2022 to 2024, he has been a Postdoctoral Research Fellow and Adjunct Professor, and he has also been involved as a Teaching Assistant for multiple engineering courses, since 2017. In 2022, he was a Visiting Scientist with the Chair of Power Electronics, Kiel University, Kiel, Germany. In 2023, he received the National Scientific Habilitation (ASN) for the permanent position of Associate Professor in Electrical Engineering. His research interests include electric vehicle chargers, photovoltaic, power electronic converters, harmonic pollution, efficiency improvement, and circuit modeling.

Dr. Mandrioli was the recipient of several awards with IEEE. He is an Associate Editor for the IEEE ACCESS and an Editorial Board Member of several journals.

Gabriele Neretti received the Ph.D. degree in electrical engineering from the University of Bologna, Bologna, Italy, in 2009.

Since 2020, he has been an Associate Professor with the Department of Electrical Electronic and Information Engineering, University of Bologna. He has authored or coauthored more than 60 international paper contributions and a book chapter, in 2016. His research interests include technological applications of nonthermal plasmas in aerospace and aeronautical domains and in the plasma medicine field. He is also involved in the design and realization of high voltage power supplies for plasma generation.

Dr. Neretti is a member of the International Society of Plasma Medicine and Editorial Board Member of the *Open Physics* and *Electronics* (MDPI).

Mattia Ricco (Senior Member, IEEE) received the master's degree (cum laude) in electronic engineering from the University of Salerno, Fisciano, Italy, in 2011, and the Ph.D. double degree in electrical and electronic engineering from the University of Cergy-Pontoise, Cergy-Pontoise, France, and in information engineering from the University of Salerno in 2015.

From 2015 to 2018, he was a Postdoctoral Research Fellow with the Department of Energy Technology, Aalborg University, Aalborg, Denmark. From 2018 to 2021, he was a Senior Assistant Professor (Tenure Track), and since 2021, he has been an Associate Professor with the Department of Electrical, Electronic, and Information Engineering, University of Bologna, Bologna, Italy. His research interests include transportation electrification, electric vehicle chargers, modular multilevel converters, battery management system, field-programmable gate array-based controllers, reliability and circularity for power electronics, and photovoltaic systems.

Dr. Ricco is an Editor for *IET Power Electronics* and an Associate Editor for the IEEE TRANSACTIONS ON INDUSTRIAL ELECTRONICS.

Open Access funding provided by 'Universita di Bologna' within the CRUI CARE Agreement